Available online at www.sciencedirect.com
SCIENCE DIRECT®
International Journal of Heat and Fluid Flow 26 (2005) 34–44
International Journal of HEAT AND FLUID FLOW
www.elsevier.com/locate/ijhff

Constructal multi-scale structure for maximal heat transfer density in natural convection

Alexandre K. da Silva, Adrian Bejan *

Department of Mechanical Engineering and Materials Science, Duke University, Box 90300, Durham, NC 27708-0300, USA

Received 10 January 2004; accepted 11 May 2004
Available online 8 July 2004

Abstract

In this paper we investigate a new design concept for generating multi-scale structures in natural convection with the objective of maximizing the heat transfer density, or the heat transfer rate per unit of volume. The flow volume is filled with vertical equidistant heated blades of decreasing lengths. The spacings between the blades are optimized for maximal heat transfer density. Smaller blades are installed in the center plane between two adjacent longer blades, in the entrance region where the boundary layers are thin and the fluid is unheated. Based on the same principle, new generations of even smaller blades are added stepwise to the multi-scale structure. Constructal theory is applied to each new generation of blades, and this method leads to the optimal spacings between blades and the optimal lengths scales. As the number of length scales increase, the flow rate and the volume-averaged heat transfer density increase. It is also shown that there is a smallest (cutoff) length scale below which the boundary layers are no longer distinct, and where the sequence of generating optimal length scales ends. The maximized heat transfer density increases as the optimized complexity of the flow structure increases.

Keywords: Constructal theory; Electronic cooling; Natural convection; Maximal heat transfer density; Packing; Compactness

1. Introduction

In design, space is at a premium. This is why the miniaturization and compactness of electronic devices is a challenge and a driving force for research. One method for generating optimal space-constrained flow configurations is constructal theory and design (Bejan, 2000; Bejan et al., 2004). According to this method, the flow configuration is free to morph in the pursuit of maximal global performance under global constraints. The resulting optimal (constructal) configuration is deduced, not assumed. It is the winner of the competition in which all the eligible configurations are simulated and compared.

One class of constructal-design configurations are the optimal internal spacings determined for heat-generating volumes cooled with channels, staggered plates, and pin fins (Bar-Cohen and Rohsenow, 1984; Bejan, 1984, 2000; Bejan and Sciubba, 1992). In each case, the total volume is fixed, the objective is to maximize the global thermal conductance of the package (or the volume-averaged heat transfer rate density), and the result is a single length scale: the optimal spacing. This length scale is distributed uniformly throughout the volume.

In the present paper we take the constructal design of optimal spacings in a new direction. Instead of a single optimal spacing, we seek an entire sequence of optimized spacings, one spacing smaller than the preceding one. We seek an optimized multi-scale flow structure that achieves even higher levels of heat transfer rate density, under the same constraints as the single-scale structures optimized in the past. The key to higher performance is the increased design freedom, because more length scales (to be optimized) represent more degrees of freedom in the design. More length scales mean that the flow structures can morph in more design directions. In the end, the optimized multiple scales are distributed nonuniformly through the available volume.

* Corresponding author. Tel.: +1-919-660-5309; fax: +1-919-660-8963.
E-mail address: dalford@duke.edu (A. Bejan).

0142-727X/$ - see front matter © 2004 Elsevier Inc. All rights reserved.
doi:10.1016/j.ijheatfluidflow.2004.05.002

Nomenclature

c_P	specific heat, J/kg K
D	spacing, m
$\widetilde{D}$	dimensionless channel spacing, Eq. (29)
g	gravitational acceleration, m/s^2
i	index
k	thermal conductivity, W/m K
L_i	lengths, m
m	smallest scale for asymmetric plates ($m+1=$ total number of length scales)
m_s	smallest scale for symmetric plates
n	number of plates
P	pressure, Pa
Pr	Prandtl number, ν/α
q'	heat transfer rate per unit length, W/m
q'''	heat transfer density, W/m^3
$\bar{q}''_0$	average heat flux, W/m^2, Eq. (7)
$\mathbf{R}$	residual vector
S	geometrical parameter
Ra	Rayleigh number, Eq. (14)
T	temperature, K
u	horizontal velocity component, m/s
$\mathbf{u}$	solutions vector
v	vertical velocity component, m/s
x, y	Cartesian coordinates, m
W	volume length, m

Greeks

α	thermal diffusivity, m^2/s
β	coefficient of volumetric thermal expansion, K^{-1}
δ	velocity boundary layer thickness, m
δ_T	thermal boundary layer thickness, m
ρ	density, kg/m^3
ν	kinematic viscosity, m^2/s
μ	viscosity, kg/s m

Subscripts

0, 1, 2	generation of multi-scale architecture
i	order of length scale
j	trial mesh
opt	optimum
max	maximum
w	wall
0	initial fluid temperature

Superscripts

$(\sim)$	dimensionless variables
n	iteration number, Eq. (39)

The multi-scale constructal design presented in this paper is for a volume cooled by laminar single-phase natural convection. We chose natural convection because it has been studied extensively (Chappidi and Eno, 1990; Anand et al., 1992; Roberts and Floryan, 1998; Kazansky et al., 2003; Auletta et al., 2003; Marcondes and Maliska, 1999), and the classical results can be used as reference (benchmark) for the new performance exhibited by optimized multi-scale structures. Furthermore, in natural convection several studies have recognized the possibility of augmenting heat transfer by inserting a smaller plate between two parallel plates (Naylor and Tarasuk, 1993a,b; Andreozzi and Manca, 2001; Andreozzi et al., 2002; Bejan and Fautrelle, 2003; Bejan et al., 2004). In this paper, we take this idea to many steps of greater complexity, analytically and numerically, and suggest that the future of augmentation and compactness belongs to optimized multi-scale flow structures that are distributed nonuniformly.

2. Constructal flow geometry

Constructal theory has been applied to the optimization of internal structure in many flow configurations (Bejan, 2000; Bejan et al., 2004). The geometry of the flow system is free to change while its global performance is being maximized. Heat and fluid flow resistances are distributed optimally through the available volume. From this process of "optimal distribution of imperfection" results the flow architecture.

Fig. 1 illustrates the principle by which resistances are distributed through a flow volume, or how heat transfer surfaces are allocated to volume elements. Thermal boundary layers develop as the fluid sweeps the heat generating surfaces, and a volume of unheated fluid appears between the boundary layers. The amount of unheated fluid depends on the shape of the total volume V. Two extreme shapes of V are shown in Fig. 1a and c. If V is too square, Fig. 1a, the unheated region is large, and the volume occupied by working fluid (the boundary layers) is small. If V is too slender, Fig. 1c, the boundary layers merge early, and the stream warms up. It becomes 'overworked', i.e., poorer as a coolant. These two extremes suggest the existence of an optimal V shape: V is occupied most fully by working fluid when its boundary layers merge at the end of the channel, Fig. 1b.

This principle is employed in Fig. 2, where a fixed two-dimensional volume $L_0 \times W$ is filled optimally with vertical plates cooled by laminar natural convection. The spacing D_0 is such that the thermal boundary layers

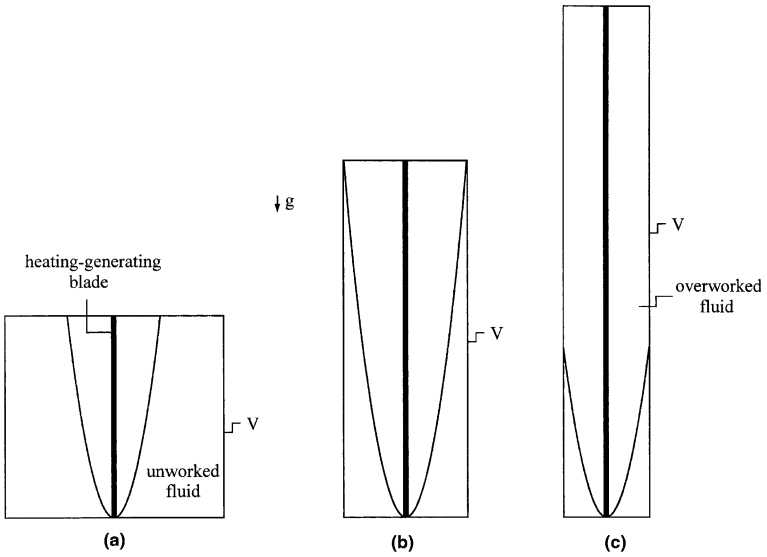

Fig. 1. The optimal volume shape for maximal heat transfer density.

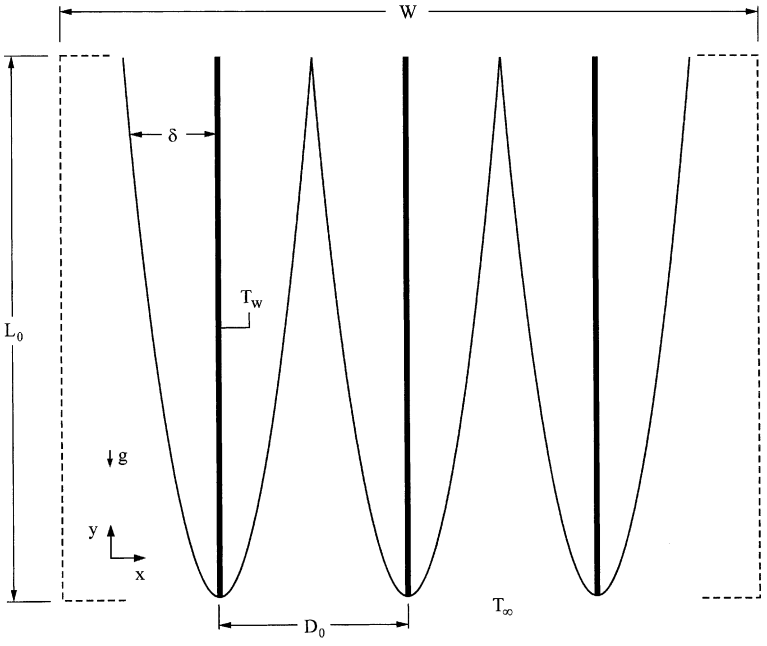

Fig. 2. Optimal package of vertical plates with one spacing.

merge at the top of the structure. Each plate has negligible thickness. The question explored in this paper is whether the performance of the parallel-plates structure can be improved beyond that of Fig. 2. The answer is yes, and it is based once more on the principle outlined in Fig. 1. The volumetric density of heat transfer can be increased by inserting heat transfer surfaces in the flow regions that contain unheated fluid, for example, in the wedges of cold fluid between the tips of two boundary layers.

The left side of Fig. 3 shows how a new plate of length L_1 is inserted in the center of the entrance to the original D_0 channel. The local spacing D_1 is equal to $D_0/2$. The new length L_1 can be predicted graphically, from the intersection of its boundary layers with the boundary layers of the L_0 plates. Reliance on such intersections is consistent with the principle of filling the available volume with "working" fluid as much as possible.

For $Pr \sim 1$, the boundary layer thickness plate scales as (e.g., Bejan, 1984),

$$\delta = \delta_T \approx y\left(\frac{g\beta(T_w - T_0)y^3}{\alpha\nu}\right)^{-1/4} \quad (1)$$

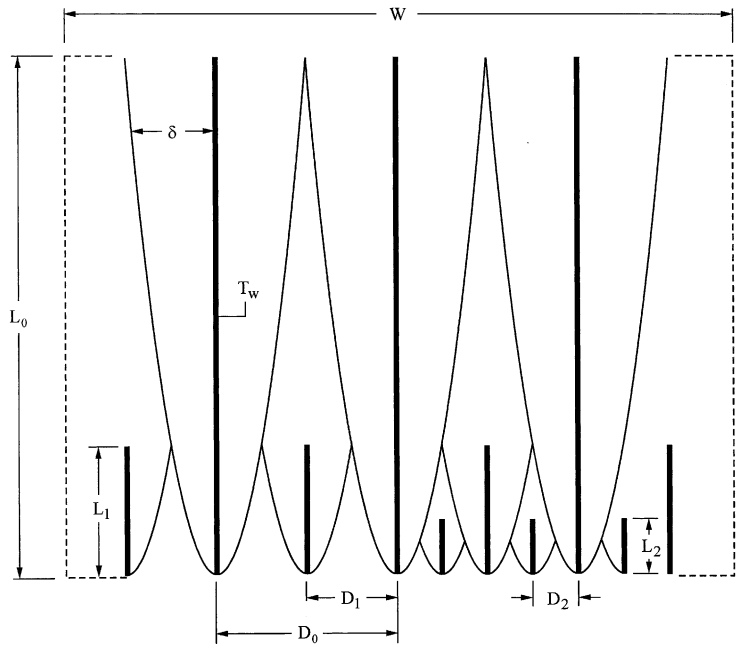

Fig. 3. The insertion of smaller plates in the unused flow.

which means that δ increases as $y^{1/4}$. The boundary layers of the L_0 and L_1 plates merge approximately at a height of $y \sim L_0/16$. This approximation yields the ratio between L_1 and L_0,

$$L_1 \cong \frac{1}{16} L_0 \tag{2}$$

The right side of Fig. 3 shows that this principle can be invoked again, if the wedge between L_0 and L_1 contains enough unheated fluid. The length of the new blade is $L_2 \cong L_1/16$. In summary, if the process of filling the flow with plates of smaller and smaller scales continues up to a small scale L_m, the length-generating algorithm is

$$L_i = \frac{1}{16} L_{i-1}, \quad D_i = \frac{1}{2} D_{i-1} \quad i = 1, 2, \ldots, m \tag{3}$$

Furthermore, the number of blades with the same size increases as the blade size decreases. In the fixed volume shown in Fig. 3, the number of L_0 blades is

$$n_0 = \frac{W}{D_0} \tag{4}$$

where

$$D_0 \cong 2\delta(L_0) \cong 2L_0 \left(\frac{g\beta(T_w - T_\infty)L_0^3}{\alpha\nu} \right)^{-1/4} \tag{5}$$

The number of blades of size L_1 is $n_1 = n_0$, because there are as many L_1 blades as there are D_0 spacings. For scales smaller than L_1, however, the number of blades doubles with every step,

$$n_i = 2n_{i-1}, \quad i = 2, 3, \ldots, m \tag{6}$$

3. Heat transfer

For the multi-scale packing constructed in Section 2, it is possible to estimate the heat transfer contribution associated with each scale by assuming that the heat transfer from each surface is equal, in order of magnitude sense, to the heat transfer through the boundary layer. For the L_0 plates, we write (cf. Bejan, 1984)

$$\frac{\bar{q}_0'' L_0}{k\Delta T} \cong 0.517 \left(\frac{g\beta\Delta T L_0^3}{\alpha\nu} \right)^{1/4} \tag{7}$$

where $\bar{q}_0''$ is the heat flux averaged over L_0, and $\Delta T = T_w - T_\infty$. Noting that each L_0 blade has two boundary layers, the total heat flux transferred from all the L_0 blades is

$$q_0' = 2n_0 \bar{q}_0'' L_0 \cong 1.034 n_0 k \Delta T \left(\frac{g\beta\Delta T L_0^3}{\alpha\nu} \right)^{1/4} \tag{8}$$

By analogy, Eq. (8) can be rewritten for every L_i smaller than L_0,

$$q_i' \cong 1.034 n_i k \Delta T \left(\frac{g\beta\Delta T L_i^3}{\alpha\nu} \right)^{1/4} \tag{9}$$

The heat transfer rate vehicled by all blades is

$$q' = \sum_{i=0}^{m} q_i' \cong 1.034 n_0 k \Delta T \left(\frac{g\beta\Delta T L_0^3}{\alpha\nu} \right)^{1/4} S \tag{10}$$

where the sum S is a geometric parameter

$$S = 1 + \frac{n_1}{n_0} \left(\frac{L_1}{L_0} \right)^{3/4} + \frac{n_2}{n_0} \left(\frac{L_2}{L_0} \right)^{3/4} + \cdots + \frac{n_m}{n_0} \left(\frac{L_m}{L_0} \right)^{3/4} \tag{11}$$

According to Eqs. (3) and (6), S increases monotonically with the number of length scales,

$$S = 1 + \frac{1}{6}(1 - 4^{-m}) \tag{12}$$

4. Heat transfer rate density

The global figure of merit of the designed flow structure is the total heat transfer rate packed in the given volume, q', or the heat transfer rate density, $q''' = q'/WL_0$. Rewriting Eq. (10) in terms of the Rayleigh number Ra

$$\frac{q'}{k\Delta T} = 1.034\frac{W}{D_0}Ra^{1/4}S \tag{13}$$

$$Ra = \frac{g\beta\Delta T L_0^3}{\alpha\nu} \tag{14}$$

we see that the heat transfer rate density increases with the Rayleigh number and with S. However, if S (or m) is too large, the spacing between the plates vanishes, and this stops the flow of coolant. The smallest scale is key, because it is the "grain" of the complex structure. To deduce the smallest scale, note that the theoretical derivation developed in Sections 2 and 3 is valid when the boundary layers are distinct, otherwise the boundary layer heat transfer mechanism will collapse. This consideration brings up the fact that boundary layers must be slender in order to be distinct, and that their slenderness decreases as their length L_i decreases. The boundary layer of rank $i = m$ is marginally slender when

$$L_m \geqslant D_m \tag{15}$$

or, according to Eq. (3), when

$$L_0 \geqslant 8^m D_0 \tag{16}$$

By substituting Eq. (5) into Eq. (16), we find that the order of magnitude of m is

$$m \leqslant \frac{\ln(Ra^{1/4}/2)}{3\ln 2} \tag{17}$$

5. Symmetrically installed plates

In this section we describe an alternative to the multiscale structure shown in Fig. 3. Instead of installing a smaller plate in the entrance formed between large plates, we install two symmetric plates around the tip of each long plate. The symmetrical structure is shown in Fig. 4, where the D_0 spacing between two long plates L_0, is occupied by two L_1 plates separated by the distance $D_1 = D_0/3$. The new boundary layers generated by the L_1 plates develop as described by Eq. (1), and merge with the L_0 boundary layers downstream at $L_1 \cong L_0/81$. Because the number of L_0 plates is n_0, the number of L_1 plates is $n_1 = 2n_0$.

As in Sections 2–4, complexity can be increased by adding pairs of smaller plates in the entrance regions. The algorithm that rules the growing symmetrical structure is

$$L_i = \frac{1}{81}L_{i-1} \tag{18}$$

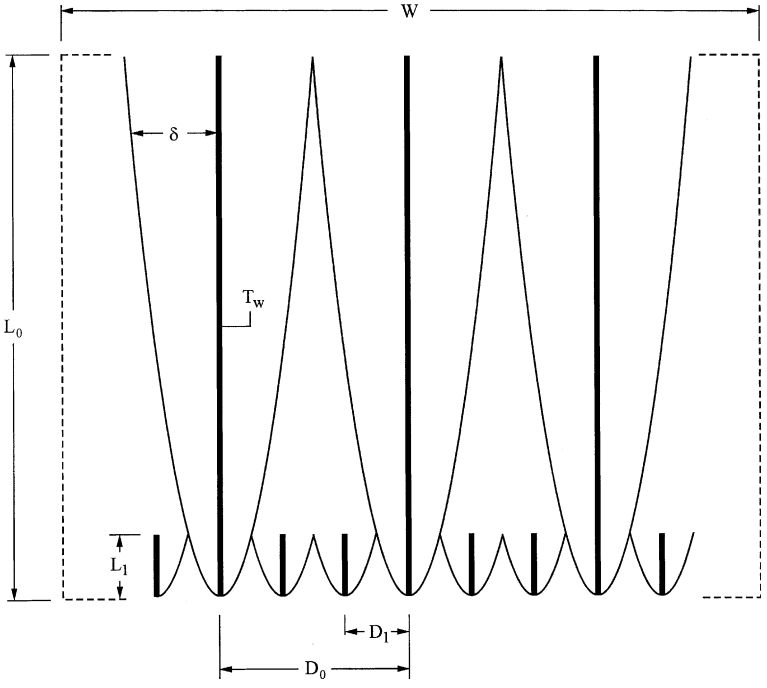

Fig. 4. Symmetrical insertion of smaller plates in the unused flow.

$$D_i = \frac{1}{3} D_{i-1} \tag{19}$$

$$n_i = 3^{i-1} 2 n_0 \tag{20}$$

where $i = 1, 2, \ldots, m_s$. The heat transfer analysis leads again to Eqs. (7)–(11), with the difference that the geometric factor S is now

$$S = 1 + \frac{1}{12}(1 - 3^{-2m_s}) \tag{21}$$

where m_s is the number of steps used in the symmetric construction. Note that m_s is different than m, which refers to the structure of Fig. 3. The subscript s refers to the symmetric construction of Fig. 4. The number m_s can be determined based on the same principle as in Eq. (15): the importance of the slenderness of the boundary layers as a "cutoff" criterion in the construction. The smallest length scale L_{m_s} cannot be smaller than

$$L_{m_s} \geqslant D_{m_s} \tag{22}$$

According to Eq. (19), $L_{m_s} = 81^{-m_s} L_0$ and $D_{m_s} = 3^{-m_s} D_0$. By using Eq. (5) for D_0 we arrive at

$$m_s \leqslant \frac{\ln(Ra^{1/4}/2)}{3 \ln 3} \tag{23}$$

Fig. 5 shows that m_s is smaller than m. The performance of the symmetrical multi-scale structure is determined by combining Eqs. (13) and (21),

$$\frac{q'_s}{k\Delta T} = 1.034 \frac{W}{D_0} Ra^{1/4} \left[1 + \frac{1}{12}(1 - 3^{-2m_s}) \right] \tag{24}$$

This can be compared with Eqs. (12) and (13), to see how the heat transfer density changes when the structure changes from Fig. 3 to Fig. 4. The ratio q'_s/q' is plotted in Fig. 6, and shows that when m increases above 2, the symmetric structure (Fig. 4) offers a heat transfer density

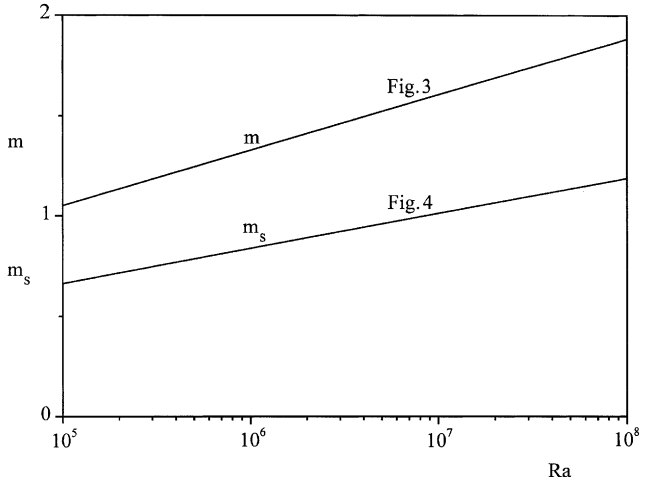

Fig. 5. Number of length scales (m, m_s) versus flow strength (Ra).

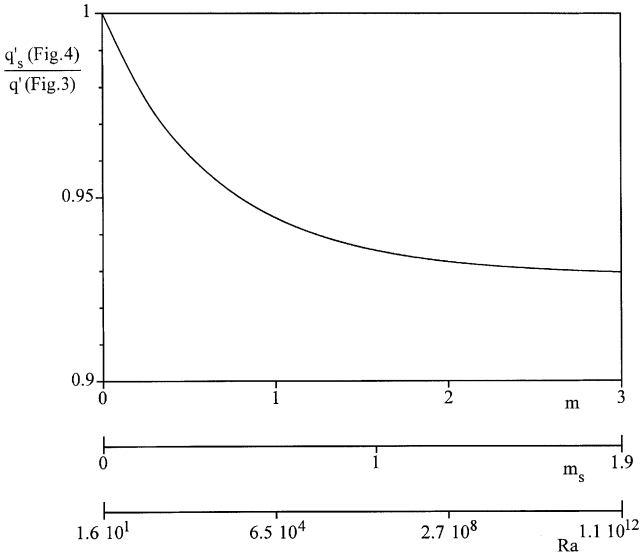

Fig. 6. Relative performance of symmetrical and asymmetrical multi-scale structures.

that is 7% smaller than in the asymmetric structure (Fig. 3). In this analytical solution, m values larger than 2 are unrealistic because Ra exceeds 10^9, and the flow regime is turbulent.

6. Numerical formulation

In the second phase of this study we optimized the multi-scale structure numerically. The computational domain is shown in Fig. 7. The walls are kept at T_w and cold fluid is drawn into the channel at T_∞. The dimensional governing equations for constant-property flow satisfying the Oberbeck–Boussinesq approximation are

$$\frac{\partial u}{\partial x} + \frac{\partial v}{\partial y} = 0 \tag{25}$$

$$\rho\left(u\frac{\partial u}{\partial x} + v\frac{\partial u}{\partial y}\right) = -\frac{\partial P}{\partial x} + \mu\nabla^2 u \tag{26}$$

$$\rho\left(u\frac{\partial v}{\partial x} + v\frac{\partial v}{\partial y}\right) = -\frac{\partial P}{\partial y} + \mu\nabla^2 v + \rho g\beta(T - T_\infty) \tag{27}$$

$$\rho c_P\left(u\frac{\partial T}{\partial x} + v\frac{\partial T}{\partial y}\right) = k\nabla^2 T \tag{28}$$

where $\nabla^2 = \partial^2/\partial x^2 + \partial^2/\partial y^2$. The variables and the fluid properties are defined in the nomenclature. It is convenient to nondimensionalize the variables,

$$(\tilde{x}, \tilde{y}, \tilde{D}, \tilde{L}) = \frac{(x, y, D, L)}{L_0} \tag{29}$$

$$(\tilde{u}, \tilde{v}) = \frac{(u, v)}{(\alpha/L_0) Ra^{1/2} Pr^{1/2}} \tag{30}$$

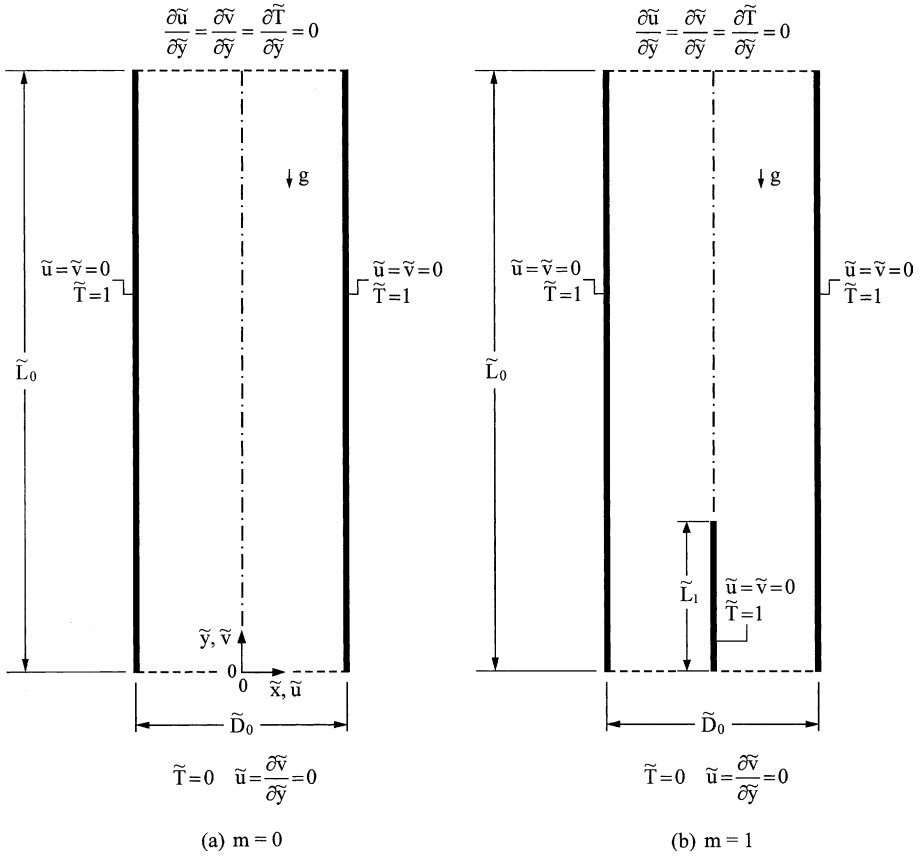

Fig. 7. Computational domain.

$$\widetilde{T} = \frac{T - T_\infty}{T_w - T_\infty} \tag{31}$$

$$\widetilde{P} = \frac{P}{(\mu\alpha/L_0^2)Ra^{1/2}Pr^{1/2}} \tag{32}$$

such that Eqs. (25)–(28) become

$$\frac{\partial \tilde{u}}{\partial \tilde{x}} + \frac{\partial \tilde{v}}{\partial \tilde{y}} = 0 \tag{33}$$

$$\left(\frac{Ra}{Pr}\right)^{1/2}\left(\tilde{u}\frac{\partial \tilde{u}}{\partial \tilde{x}} + \tilde{v}\frac{\partial \tilde{u}}{\partial \tilde{y}}\right) = -\frac{\partial \widetilde{P}}{\partial \tilde{x}} + \nabla^2\tilde{u} \tag{34}$$

$$\left(\frac{Ra}{Pr}\right)^{1/2}\left(\tilde{u}\frac{\partial \tilde{v}}{\partial \tilde{x}} + \tilde{v}\frac{\partial \tilde{v}}{\partial \tilde{y}}\right) = -\frac{\partial \widetilde{P}}{\partial \tilde{y}} + \nabla^2\tilde{v} + \left(\frac{Ra}{Pr}\right)^{1/2}\widetilde{T} \tag{35}$$

$$(RaPr)^{1/2}\left(\tilde{u}\frac{\partial \widetilde{T}}{\partial \tilde{x}} + \tilde{v}\frac{\partial \widetilde{T}}{\partial \tilde{y}}\right) = \nabla^2\widetilde{T} \tag{36}$$

The boundary conditions are indicated on Fig. 7a for one length scale, and Fig. 7b for two length scales. The walls are impermeable with no-slip ($\tilde{u} = \tilde{v} = 0$) and at constant temperature, $\widetilde{T} = 1$. As the flow configuration is a sandwich of boundary layers, the slenderness of the channel is a consequence of the optimization process, and this allows us to assume on the entrance plane ($\tilde{y} = 0$) uniform velocity profile ($\tilde{u} = 0$), ($\partial\tilde{v}/\partial\tilde{y} = 0$, as required by mass conservation) and isothermal fluid ($\widetilde{T} = 0$). The velocity and temperature boundary conditions on the outlet plane are $\partial\tilde{u}/\partial\tilde{y} = \partial\tilde{v}/\partial\tilde{y} = \partial\widetilde{T}/\partial\tilde{y} = 0$. These boundary conditions are a realistic approximation for slender channels in the high Rayleigh number regime. The same flow and temperature boundary conditions were used for simulating more complex configurations ($m \geqslant 2$). Symmetry was used in all the numerical simulations. The boundary conditions on the plane of symmetry were $\tilde{u} = \partial\tilde{v}/\partial\tilde{x} = \partial\widetilde{T}/\partial\tilde{x} = 0$. This allowed us to discretize only half of the flow domain, and use a zero-thickness for the second plate of length $\widetilde{L}_1$. This saved a significant amount of grid work for structures with $m = 1$. The thickness of the $\widetilde{L}_1$ plate was also set to zero in structures with $m = 2$, where the dimensionless thickness of the $\widetilde{L}_2$-long plate was set equal to 10^{-4}.

The flow and the temperature field were simulated for several configurations, one differing slightly from the next, in order to determine the overall heat transfer density. The figure of merit is based on the total rate of heat transfer from the plates to the fluid,

$$q' = k\int_0^{L_0}\left(\frac{\partial T}{\partial x}\right)_{x=D_0/2}\mathrm{d}y - k\int_0^{L_0}\left(\frac{\partial T}{\partial x}\right)_{x=-D_0/2}\mathrm{d}y + \sum_{i=1}^{m} n_i\left[k\int_0^{L_i}\left(\frac{\partial T}{\partial x}\right)_{x=D_i^+}\mathrm{d}y - k\int_0^{L_i}\left(\frac{\partial T}{\partial x}\right)_{x=D_i^-}\mathrm{d}y\right] \quad (37)$$

where $(m+1)$ is the number of length scales. The dimensionless overall heat transfer density $(q''' = q'/L_0D_0)$ is

$$\tilde{q} = \frac{q'''L_0^2}{k(T_w - T_\infty)} \quad (38)$$

Eqs. (25)–(28) were solved using a finite element code (FIDAP, 1998). The numerical domain was discretized nonuniformly using quadrilateral elements with 9 nodes each one. The explicit appearance of the pressure was eliminated based on a penalty function, with an error factor set at 10^{-8}. The nonlinear equations resulting from the Galerkin finite element method were solved by successive substitutions and Newton–Raphson scheme. The upwind formulation was applied in order to control spatial numerical instabilities generated at high *Ra*. The convergence criteria were

$$\frac{\|\mathbf{u}^{(n)} - \mathbf{u}^{(n-1)}\|}{\|\mathbf{u}^{(n)}\|} \leqslant 0.001 \quad \text{and} \quad \frac{\|\mathbf{R}(\mathbf{u}^{(n)})\|}{\|\mathbf{R}_0\|} \leqslant 0.001 \quad (39)$$

Because of the presence of boundary layers, the mesh design received special attention and was exhaustively tested. The grid refinement test for a simple channel (Fig. 7a) shows that the solution becomes mesh independent if a nonuniform grid is used in the $\tilde{x}$ direction, and a uniform grid is used in the $\tilde{y}$ direction, with the smaller elements located close the verticals walls to capture the thermal boundary layers. The initial guess used for the grid size in $\tilde{x}$ direction was the boundary layer thickness scale, $\delta \approx L_0Ra^{-1/4}$. The mesh study showed that for $Ra = 10^5$ and 10^6, the heat flux density was insensitive to further grid refining if 101 nodes per unit of length were used in both directions. For $Ra = 10^7$ and 10^8, 201 nodes per L were used in both directions. This means that if we were simulating the channel $\widetilde{L}_0 = 1$, $\widetilde{D}_0 = 0.15$ for $Ra = 10^5$ and 10^6, the grid had 101 nodes in the $\tilde{y}$ direction and 15 nodes in the $\tilde{x}$ direction. However, to simulate the same channel for $Ra = 10^7$ and 10^8, 201 nodes are required in the $\tilde{y}$ direction, and 31 nodes in the $\tilde{x}$ direction. Table 1 shows one example of how grid independence was achieved for $Ra = 10^5$, $Pr = 0.7$, and $\widetilde{D} = 0.15$.

Grid refinement tests showed that the non-uniform grid was necessary in both directions, especially as the number of scales increases (e.g., Fig. 7b). The grid in the $\tilde{x}$ direction was generated as follows: 201 nodes per L for $Ra = 10^5$, 301 nodes for $Ra = 10^6$, and 401 nodes for $Ra = 10^7$–10^8. In order to capture the boundary layers on the auxiliary plate, the domain was divided in such a way that the smallest elements were always close to the wall. In the $\tilde{y}$ direction, the grid had 201 nodes along $\widetilde{L}_0$, and was double-graded uniformly from $0 \leqslant \tilde{y} \leqslant L_1$ for $Ra = 10^5$. For $Ra = 10^6$, 301 nodes were used along $\widetilde{L}_0$, and the grid was triple-graded uniformly for $0 \leqslant \tilde{y} \leqslant \widetilde{L}_1$. For $Ra = 10^7$ and 10^8, the grid had 401 nodes along $\widetilde{L}_0$, and was quadruple-graded along $0 \leqslant \tilde{y} \leqslant L_1$. For example, in the simulation of the channel $(\widetilde{L}_0 = 1, \widetilde{D}_0 = 0.15)$ at $Ra = 10^5$, with one auxiliary plate $(\widetilde{L}_1 = 0.1)$ located at $\tilde{x} = 0$, the grid had 15 nodes in the range $-\widetilde{D}_0/2 \leqslant \tilde{x} \leqslant 0$, 15 nodes in the range $0 \leqslant \tilde{x} \leqslant \widetilde{D}_0/2$, 41 nodes distributed uniformly from $0 \leqslant \tilde{y} \leqslant \widetilde{L}_1$, and 161 nodes for $\widetilde{L}_1 \leqslant \tilde{y} \leqslant \widetilde{L}_0$. For $Ra = 10^7$ and 10^8, the grid had 61 nodes in $\tilde{x}$ direction, 81 nodes along $0 \leqslant \tilde{y} \leqslant \widetilde{L}_1$ and 321 nodes along $\widetilde{L}_1 \leqslant \tilde{y} \leqslant \widetilde{L}_0$. This procedure was adopted for all the configurations reported in this paper.

Table 1
Grid refinement test

Nodes	Elements	$\tilde{q}$	$\left\|\frac{\tilde{q}^j - \tilde{q}^{j+1}}{\tilde{q}^{j+i}}\right\|$
707	250	141.625	–
1161	384	143.858	0.0155
1749	553	145.576	0.0119
2431	744	147.062	0.0102
3255	972	148.269	0.0082

7. Discussion

The search for the maximum heat transfer density started with the simplest structure possible (one length scale, L_0, or $m = 0$). In this case, there is only one degree of freedom, D_0. The optimal spacing was found by fixing the Rayleigh number $(Ra = 10^5$–$10^8)$ and the Prandtl number $(Pr = 0.7)$, and then varying $\widetilde{D}_0$. The result for $\widetilde{D}_{0,\mathrm{opt}}$ was compared with the available literature, in order to validate the numerical code. The procedure was repeated several times to cover the range $10^5 \leqslant Ra \leqslant 10^8$. Fig. 8 shows that the plate-to-plate spacing has a strong effect on the heat transfer density. The axes of Fig. 8 are nondimensionalized according to the theoretical solutions presented in Bejan (1984, 2000),

$$\widetilde{D}_{\mathrm{opt}}Ra^{1/4} \approx 2.3 \quad (40)$$

$$\tilde{q}_{\max}Ra^{-1/2} \geqslant 0.45 \quad (41)$$

The figure shows that the optimum plate-to-plate spacing, which corresponds to the heat transfer density peak, is located between 2 and 3 on the abscissa, which is in good agreement with Eq. (40). The heat transfer density reaches a maximum at $\tilde{q}Ra^{-1/2} = 0.443$, which is very close to the theoretical prediction, Eq. (41).

A consistent global optimization method had to be used as the number of length scales present in the multiscale structure increased. For cases in which one L_1 plate

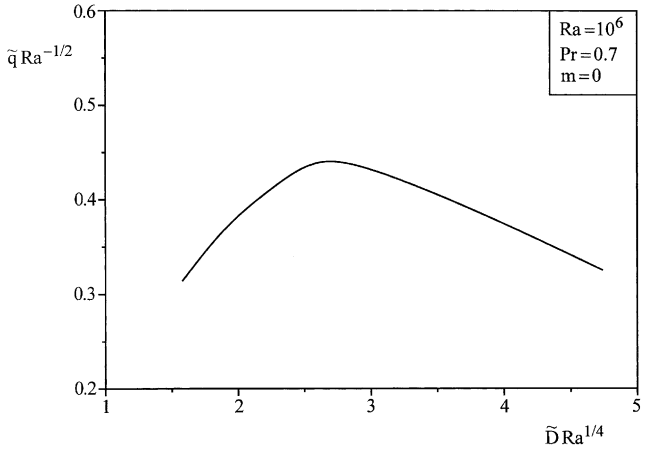

Fig. 8. The effect of the plate-to-plate spacing on the heat transfer density.

is inserted in the center of the entrance zone of the L_0-long channel ($m = 1$), the optimization process was performed in two nested loops, because of the two degrees of freedom: $\widetilde{D}_0$ and $\widetilde{L}_1$. In the inner loop, the values for Ra, Pr, and $\widetilde{L}_1$ were specified, and $\widetilde{D}_0$ was varied until $\tilde{q}_{\max}$ was reached. The outer loop required that the inner loop was repeated for many values of $\widetilde{L}_1$, such that all the possible combinations of $\widetilde{D}_0$ and $\widetilde{L}_1$ were considered. The result, $\tilde{q}_{\max}$ ($m = 1$), was 'twice maximized' because it was maximized with respect to both $\widetilde{L}_1$ and $\widetilde{D}_0$. The same procedure was performed for cases where $m = 2$, where the degrees of freedom were three: $\widetilde{D}_0$, $\widetilde{L}_1$ and $\widetilde{L}_2$.

Fig. 9 shows a summary of the dimensionless optimal spacing for $m = 0$, 1 and 2. Note that $\widetilde{D}_{0,\mathrm{opt}}$ increases slightly with m, and cannot be correlated as in Eq. (40). The number of length scales has two effects on the optimum spacing, which are represented by the power law correlation

$$\widetilde{D}_{0,\mathrm{opt}} \cong aRa^{-r} \tag{42}$$

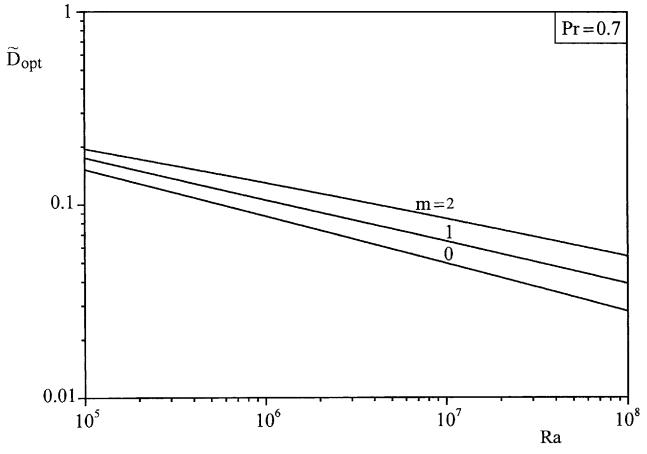

Fig. 9. The effect of complexity (m) on the optimal spacing.

where parameters a and r are functions of the number of scales. The factor a increases with the number of length scale, and the factor r decreases as m increases. The disagreement between Eq. (40) and the results obtained numerically for configurations in which $m > 0$ is minor, and this shows that Eq. (40) is a robust result.

Fig. 10 shows the optimized length scales of the smaller plates for $m = 1$ and 2. All length scales increase with Ra. The slenderness of the channel also increases in this direction. An important feature is that $\widetilde{L}_{1,\mathrm{opt}}$ and $\widetilde{L}_{2,\mathrm{opt}}$ agree in order of magnitude with Eq. (3). Another interesting finding is that $\widetilde{L}_{1,\mathrm{opt}}(m = 1)$ is greater than $\widetilde{L}_{1,\mathrm{opt}}(m = 2)$. In other words, the optimized length L_1 is shorter when smaller plates (L_2) are inserted.

Fig. 11 shows the variation of the maximal heat transfer density for $m = 0$, 1 and 2. Diminishing returns are evident: the difference between the $\tilde{q}_{\max}$ values of two consecutive multi-scale structures decreases as m increases. The average heat transfer density increases by

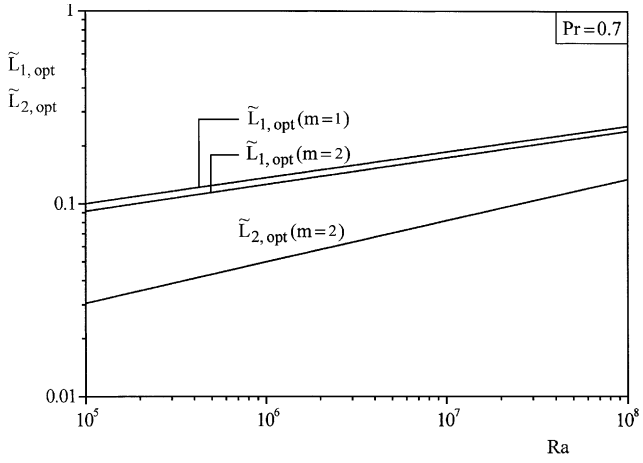

Fig. 10. The optimized lengths of packages with two and three length scales.

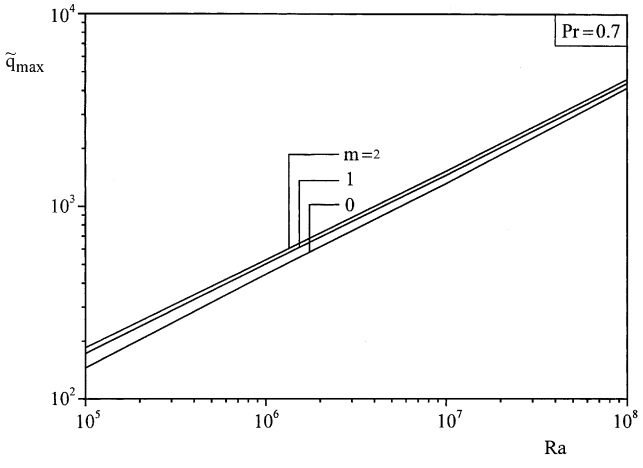

Fig. 11. The maximized heat transfer density of packages with one, two and three length scales.

12% from the simplest structure ($m = 0$) to one with two length scales ($m = 1$), and by 6% from $m = 1$ to $m = 2$. This feature was anticipated theoretically in Eq. (18), where an asymptotic behavior for q' was observed. However, it is more useful to express Eq. (18) in terms of maximum heat transfer density, by setting $\widetilde{D}_0 = \widetilde{D}_{0,\mathrm{opt}}$ in Eq. (18), where $\widetilde{D}_{0,\mathrm{opt}}$ is given by Eq. (40):

$$\tilde{q}_{\max} Ra^{-1/2} \cong 0.45\left[1 + \frac{1}{6}(1 - 4^{-m})\right] \tag{43}$$

Fig. 12 shows a comparison between the theoretical solution, Eq. (43), and the numerical maximal heat transfer density. The agreement is good in an order of magnitude sense. Both solutions exhibit the correct asymptotic trend as m increases. Diminishing returns are also observed as m increases. Furthermore, in structures

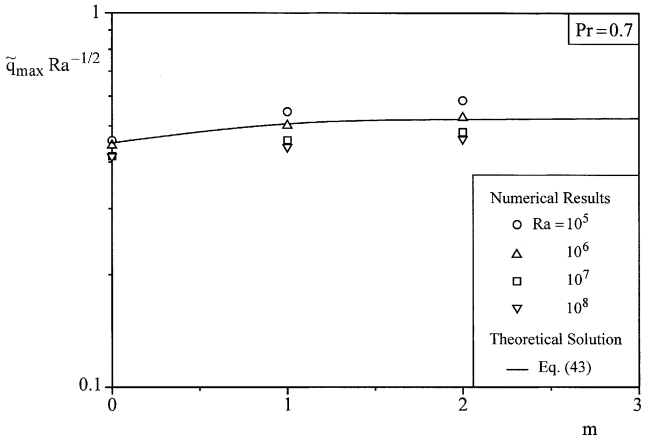

Fig. 12. Maximum heat transfer density versus number of scales: comparison between the theoretical solution and the numerical results.

with $m > 2$ the theoretical maximum heat transfer density reaches a plateau with no substantial gain for additional complexity. The plateau can be related to the cutoff anticipated in Eq. (17), which states that the heat transfer density gain associated with increasing complexity is zero at $m \cong 1$ when $Ra = 10^5$, and at $m \cong 2$ when $Ra = 10^8$. According to Eq. (17), when Ra reaches 10^5 the structure is close to the cutoff region, because we have reached numerically configurations with $m = 2$. This means that when $Ra = 10^5$ the insertion of a new generation of smaller length scales (L_3) will not change the heat transfer density significantly.

Fig. 13 shows the numerical temperature distribution inside a section of the WL_0 space of Fig. 2, for three optimized structures: $m = 0$, 1 and 2, at $Ra = 10^6$ and $Pr = 0.7$. The section consists of only four L_0-long channels. The temperature ranges between two main colors, red ($\widetilde{T} = 1$) and blue ($\widetilde{T} = 0$). As the number of length scales increases, the color red is distributed more uniformly, illustrating the progress towards maximal heat transfer rate density, or "optimal distribution of imperfection" (Bejan, 2000).

8. Conclusions

In this paper we presented and evaluated a concept for maximizing the heat transfer rate density in a fixed volume cooled by natural convection. The notion of optimal plate-to-plate spacings, known from earlier studies, was used to generalize the concept, and to develop a sequence of optimal spacings. The opportunity for performing better than the one-optimal-spacing structure comes from the observation that in the

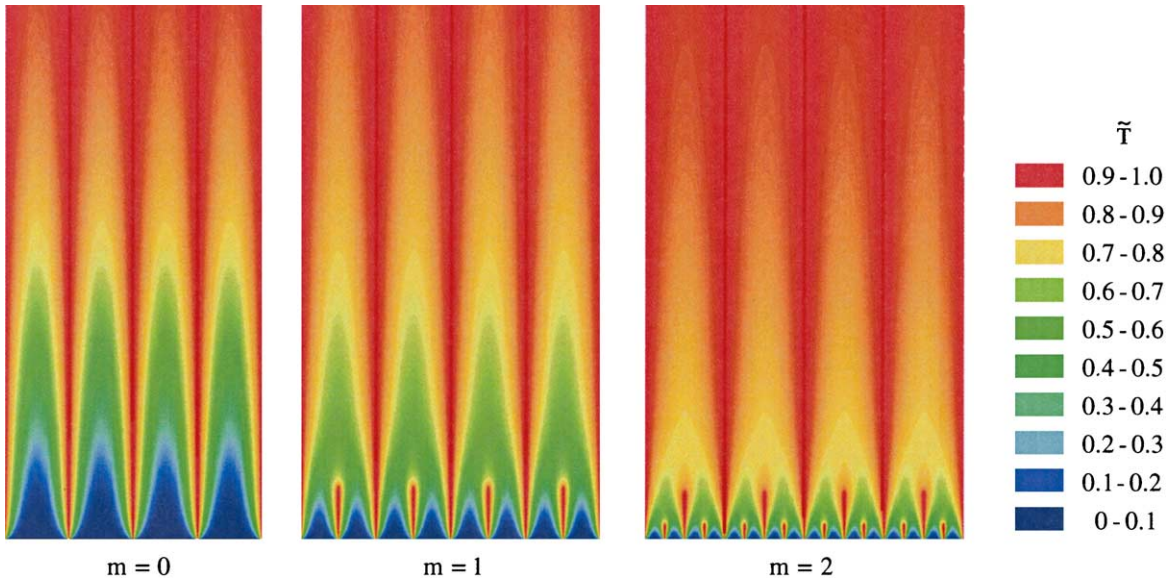

Fig. 13. The temperature distribution in packages with one, two and three length scales.

entrance between parallel plates there is a volume of unused flow: isothermal fluid that has not interacted with the plates yet. It is in this unused volume that the designer inserts new plates of appropriately smaller size.

According to the numerical results, the improvement in global performance associated with the optimal insertion of the first and second generations of smaller plates was significant, increasing the heat transfer density by about 12% and 6%, respectively. Diminishing results were also evident, showing that the contribution of each new generation of plates is less important than the contribution of the preceding generation.

The act of refining the structure near the entrance plane (Fig. 13) continues until the newest and smallest plates are so small that boundary layers are no longer distinct. The smallest scale plays the role of cutoff. The number of distinct length scales increases as $\ln Ra^{1/4}$ as the flow strength (Ra) increases. The design sequence of adding new length scales is guided by the shape of the core fluid in each entrance region: new plates are inserted in every such region.

In this new paper, the new concept was presented in the simplest situation, namely the limit where the horizontal dimension of the available space (W, Fig. 2) is much larger than the largest spacing (D_0). In this limit the number of L_0-long channels is large, and all the channels are the same, cf. the element studied numerically in Fig. 7. When W is not much larger than D_0, the number of L_0 plates is not large, and the effect of the vertical walls of the W-wide space becomes significant. In conclusion, an important future extension of this paper would be to study and optimize numerically multi-scale flow structures in which the number of the largest lengths is small. Such studies will show that the optimized architectures reported in this paper continue to hold (as approximate, nearly optimal structures) even when the lateral walls have an effect. Such robustness, which is evident in other multi-scale flow structures (e.g., trees, Bejan, 2000) deserves to be studied and documented.

Acknowledgements

A.K. da Silva acknowledges the support received from CNPq—Conselho Nacional de Desenvolvimento Cientifico e Tecnológico, Brazil. A. Bejan's work was supported by National Science Foundation.

References

Anand, N.K., Kim, S.H., Fletcher, L.S., 1992. The effect of plate spacing on free-convection between heated parallel plates. J. Heat Transfer 114, 515–518.

Andreozzi, A., Manca, O., 2001. Thermal and fluid dynamic behavior of symmetrically heated vertical channel with auxiliary plate. Int. J. Heat Fluid Flow 22, 424–432.

Andreozzi, A., Manca, O., Naso, V., 2002. Natural convection in vertical channels with an auxiliary plate. Int. J. Numer. Methods Heat Fluid Flow 12, 716–734.

Auletta, A., Manca, O., Musto, M., Nardini, S., 2003. Thermal design of symmetrically and asymmetrically heated channel-chimney systems in natural convection. Appl. Therm. Eng. 23, 605–621.

Bar-Cohen, A., Rohsenow, W.M., 1984. Thermally optimum spacing of vertical, natural convection cooled parallel plates. J. Heat Transfer 116, 116–123.

Bejan, A., 1984. In: Convection Heat Transfer. Wiley, New York, p. 1984. p. 157, Problem 11(2nd ed., 1995, pp. 132–136, 202–205).

Bejan, A., 2000. Shape and Structure, from Engineering to Nature. Cambridge University Press, Cambridge, UK.

Bejan, A., Fautrelle, Y., 2003. Constructal multi-scale for maximal heat transfer density. Acta Mech. 163, 39–49.

Bejan, A., Sciubba, E., 1992. The optimal spacing of parallel plates cooled by forced convection. Int. J. Heat Mass Transfer 35, 3259–3264.

Bejan, A., Dincer, I., Lorente, S., Miguel, A.F., Reis, A.H., 2004. Porous and Complex Flow Structures in Modern Technologies. Springer-Verlag, New York.

Chappidi, P.R., Eno, B.E., 1990. A comparative-study of the effect of inlet conditions on a free-convection flow in a vertical channel. J. Heat Transfer 112, 1082–1085.

FIDAP, 1998. Fluid Dynamics International, Evanston, IL.

Kazansky, S., Dubovsky, V., Ziskind, G., Letan, R., 2003. Chimney-enhanced natural convection from a vertical plate: experiments and numerical simulations. Int. J. Heat Mass Transfer 46, 497–512.

Marcondes, F., Maliska, C.R., 1999. Treatment of the inlet boundary conditions in natural-convection in open-ended channels. Numer. Heat Transfer Part B 35, 317–345.

Naylor, D., Tarasuk, J.D., 1993a. Natural convective heat transfer in a divided vertical channel, Part 1, Numerical Study. J. Heat Transfer 115, 377–387.

Naylor, D., Tarasuk, J.D., 1993b. Natural convective heat transfer in a divided vertical channel, Part 2, Experimental study. J. Heat Transfer 115, 388–394.

Roberts, D.A., Floryan, J.M., 1998. Heat transfer enhancement in the entrance zone of a vertical channel. J. Heat Transfer 120, 290–291.